Int. J. Environ. Sci. Technol. (2015) 12:1845–1856
DOI 10.1007/s13762-014-0535-x

ORIGINAL PAPER

Ferrous oxalate, maghemite and hematite nanorods as efficient adsorbents for decontamination of Congo red dye from aqueous system

J. P. Dhal · B. G. Mishra · G. Hota

Received: 25 January 2013 / Revised: 10 November 2013 / Accepted: 17 February 2014 / Published online: 15 March 2014

Abstract In this present study, we have synthesized ferrous oxalate nanorods by a modified co-precipitation methods. The obtained nanomaterial (ferrous oxalate nanorod) was calcined at higher temperatures to form both maghemite and hematite nanorods. The morphology, size, crystalline phases, formation and surface area of the nanorods were characterized by scanning electron microscope, transmission electron microscope, X-ray diffraction, Fourier transform infrared spectroscope, ultraviolet–visible diffuse reflectance spectroscope and Brunauer–Emmett–Teller surface area analytical techniques. The results showed that high-yield aligned nanorods with a typical diameter of 100–200 nm and length up to micrometers were formed. The obtained rod-shaped nanomaterials (i.e., ferrous oxalate, maghemite and hematite) were used as adsorbents and were applied to remove Congo red (CR) dye molecules, which was used as a model of organic pollutants in aqueous solution. The adsorption isotherms and kinetics of removal of CR were studied. It was found that the adsorption capacity of maghemite nanorod is highest among the three adsorbents and can be regarded as an effective adsorbent for removal of CR from aqueous solution.

Keywords Co-precipitation method · Nanomaterials · Nanorod · Congo red (CR) · Adsorption

Introduction

Water pollution is a major global problem which is the leading worldwide cause of deaths and diseases. Many synthetic chemicals are extremely resistant to biodegradation by native microorganisms and are major water pollutants, such as pesticides, organochlorines, polychlorinated biphenyls, polycyclic aromatic hydrocarbons, wood preservatives, synthetic polymers and synthetic dyes. Synthetic dyes are extensively used in different industries, including paper, plastic, leather, pharmaceutical, food, cosmetic, dyestuff and textile industries (Ge et al. 2012; Haider et al. 2011). Dyeing is a fundamental operation during the textile fiber processing. This operation causes the production of more or less colored waste waters, depending on the degree of fixation of the dyes on the substrates, which varies with the nature of the substances, the desired intensity of coloration and the application method (Wawrzkiewicz 2012). According to a recent study, approximately 700,000 tons of different dyes are produced annually in the world, and more than 60 % of the world dye production is consumed by textile industries (Hu et al. 2010a, b). Due to the presence of hazardous wastes and toxic pollutants in the effluents from the textile industry, they are highly problematic to environment. Among them, organic dyes are one of the major groups of pollutants in waste waters. These toxic dyes have significant impact on the human health and the aquatic life. The used dyes may cause an eco-toxic hazard and induce the potential danger of bioaccumulation (Toor and Jin 2012; Wang et al. 2012a, b; Kumar and Bansal 2012).

The toxic nature of dye is that on decomposition it gives hazardous products such as carbon dioxide, carbon monoxide, nitrogen oxide and hydrogen chloride. These products are toxic and causes severe health problem to living beings (Irama et al. 2010). Congo red [1-naphthalene sulfonic acid, 3, 30-(4, 40-biphenylenebis(azo))bis(4-amino-) disodium salt] an anionic dye has been known to cause an allergic reaction and to be metabolised to benzidine, a human carcinogen. Congo red (CR) mainly occurs in the

J. P. Dhal · B. G. Mishra · G. Hota (✉)
Department of Chemistry, N.I.T. Rourkela, Rourkela, Odisha, India
e-mail: garud31@yahoo.com

effluents discharged from textile, paper, printing, leather industries, etc. Its molecular formula is $C_{32}H_{22}N_6Na_2O_6S_2$ (Yosef and Avnir 2011; Chatterjee et al. 2010).

There are several methods for removal of organic dyes from aqueous solution such as coagulation (Marechal et al. 1997), nanofiltration (Chakraborty et al. 2003), ozonation (Khadhraoui et al. 2009), ultrasound irradiation (Song et al. 2009), ion exchange (Wawrzkiewicz and Hubicki 2010), activated carbon filter (Chan et al. 2009), oxidation (Lucas and Peres 2006), membrane processes (Sachdeva and Kumar 2009), micellar-enhanced ultrafiltration (Purkait et al. 2004) and adsorption (Wang et al. 2012a, b). Among all the processes, adsorption is a very effective separation technique and now it is considered as superior to other techniques for water treatment in terms of effectiveness, initial cost, simplicity of design, and ease of operation and insensitive to toxic substances and its environmentally friendly reasons. Similarly, this technique can handle fairly large flow rates, producing a high-quality effluent that does not result in the formation of harmful substances, such as ozone and free radicals. In this process, the dye species are transferred from the water effluent to a solid phase that leads to decrease the effluent volume (Dawood and Sen 2012; Toor and Jin 2012; Wang et al. 2012a, b; Zhu et al. 2012a, b).

Many researchers used various adsorbent for removal of CR from aqueous solution such as fly ash (Dizge et al. 2008), bentonite (Lian et al. 2009), montmorillonite (Wang and Wang 2008), chitosan (Chatterjee et al. 2009), organo-attapulgite (Chen and Zhao 2009), activated carbon (Lorenc-Grabowska and Gryglewicz 2007; Namasivayam and Kavitha 2002; Purkait et al. 2007), bottom ash and deoiled soya (Mittal et al. 2009), Azadirachta indica leaf powder (Bhattacharyya and Sharma 2004), Trametes versicolor (Binupriya et al. 2008), jute stick powder (Panda et al. 2009), Aspergillus niger (Fu and Viraraghavan 2002), cattail root (Hu et al. 2010a, b), anilinepropylsilica xerogel (Pavan et al. 2008), perlite (Vijayakumar et al. 2009), sawdust (Jain and Sikarwar 2008), rice husk ash (Chowdhury et al. 2009), mesoporous hematite (α-Fe_2O_3) (Yu et al. 2008) and CNTs/β-FeOOH (Song et al. 2012). However, some of these adsorbents do not have good adsorption capacities for anionic dyes. Nowadays, research focused on the use of nanotechnology for environmental clean-up/remediation. Arising out of their ultrafine size, large surface area and interface-dominated properties, nano-sized materials can be used to decontaminate the toxic organic and inorganic chemical from the environments. Recently, Afkhami and Moosavi (2010) used maghemite nanoparticle, prepared by co-precipitation method, for removal of CR from aqueous solution.

In the present investigation, by using a modified wet chemical method, we have prepared different 1-dimensional nano-adsorbents such as ferrous oxalate ($FeC_2O_4 \cdot 2H_2O$) nanorod, hematite (α-Fe_2O_3) nanorod and maghemite (γ-Fe_2O_3) nanorod. The prepared adsorbents were employed for removal of CR, and a comparative study was carried out by evaluating equilibrium isotherms and kinetic data for selection of the most effective adsorbent among them. The advantages of using iron oxide nanomaterials as adsorbents are as follows: They are most stable material under ambient conditions and have a great scientific and technological importance because of their n-type semiconducting properties with their narrow band gap around 2 eV, chemical stability and nontoxicity.

This research work was carried out in Rourkela, India, during the period of March 2012 to November 2012.

Materials and methods

Materials

Congo red (CR, molecular formula $C_{32}H_{22}N_6Na_2O_6S_2$, molecular weight 696.66 g mol^{-1}, $\lambda_{max} = 498$ nm), an anionic azo dye, obtained from Merck (India) was selected as dye.

Synthesis of adsorbent

All chemicals used in the investigation such as Ferrous sulfate heptahydrate, oxalic acid dihydrate, CTAB and ethanol were of analytical grade and were used without further purification. The chemicals were obtained from Merck (India).

Ferrous sulfate heptahydrate ($FeSO_4 \cdot 7H_2O$) was dissolved in 10 mL of double-distilled water with intensive stirring to form solution-A. Oxalic acid dihydrate ($H_2C_2O_4 \cdot 2H_2O$) and CTAB (Cetyl trimethylammonium bromide) were dissolved in 25 mL of ethanol with intensive stirring to form solution-B. Then, solution-A was added to solution-B with intensive stirring to form a yellow colored homogeneous solution. After addition, the stirring was carried out for another 5 h. Then, the yellow colored precipitate obtained was centrifuged, washed thoroughly by ethanol and double-distilled water and dried at 80 °C for 2 h to form $FeC_2O_4 \cdot 2H_2O$ nanorod. A part of this nanopowder was heated at 300 °C in moist condition to obtained γ-Fe_2O_3 nanorod and heated at 550 °C to obtained α-Fe_2O_3 nanorod.

Characterization of adsorbent

Various characterization techniques were used to characterize the 1-D nanoadsorbents. The crystalline phases were identified by mean of X-ray diffraction (XRD) by a PANalytical X-ray diffractometer with Cu Kα radiation (λ) 1.54156 Å at a scan rate of 2°/min. The surface morphology of the prepared adsorbent materials was characterized by a JEOL JSM-5300 scanning electron microscope (SEM) operated at an acceleration voltage of 15 and 20.0 kV. The size of the particle and selected area electron diffraction (SAED) pattern of the dried γ-Fe_2O_3 powder were observed using a high-resolution transmission electron microscope (TEM) (JEM-2100 HRTEM, Make-JEOL, Japan) with an acceleration voltage of 200 kV. Fourier transform infrared spectroscopy (FTIR) results were recorded using Perkin-Elmer FTIR (Spectrum RX-I) spectrophotometer. The ultraviolet–visible diffuse reflectance spectra (UV–Vis DRS) of the sample were recorded using Shimadzu spectrometer (model 2450) with $BaSO_4$ coated integration sphere in the range of 200–800 nm. Specific surface area and pore size distribution (PSD) were determined by the Brunauer–Emmett–Teller (BET) and Barrett–Joyner–Halenda (BJH) methods, respectively, by N_2 adsorption–desorption technique by automated surface area and porosity analyser (COULTER SA 3100 Series Surface Area and Pore Analyzers). Prior to the analysis, sample was degassed under a vacuum (1×10^{-5} Torr) at 150 °C for 1.5 h.

Adsorption experiment

For the removal of CR dye from water, the adsorption experiments were carried out using the three prepared adsorbents: $FeC_2O_4 \cdot 2H_2O$, α-Fe_2O_3 and γ-Fe_2O_3 nanorods. A stock solution of CR (1 g L^{-1}) was prepared in double-distilled water, and desired concentrations of the dye were obtained by diluting the same with double-distilled water. The calibration curve of CR was prepared by measuring the absorbance of different concentrations of the samples at $\lambda_{max} = 498$ nm using UV–vis spectrophotometer, as CR has a maximum absorbance at wavelength 498 nm on a UV–vis spectrophotometer.

Figure 1 shows the UV–vis spectra of CR solutions of concentration 100 mg L^{-1} before and after adsorption using 0.05 g of different adsorbents, such as $FeC_2O_4 \cdot 2H_2O$ nanorod, γ-Fe_2O_3 nanorod and α-Fe_2O_3 nanorod with reaction time 30 min. At a γ-Fe_2O_3 dosage of 0.05 g^{-1}, the colloidal suspension is able to adsorb almost 100 % of CR (Fig. 1), and the photograph of before and after adsorption also confirms the removal of the CR at this dosage of γ-Fe_2O_3 (Fig. 1, inset).

The amount of adsorption q_e is calculated by equation (Nethaji et al. 2012):

$$q_e = \frac{C_0 - C_e}{w} V \quad (1)$$

where q_e is the amount of adsorption at equilibrium in mg g^{-1}, C_0 and C_e are the initial and equilibrium concentration of the dye in mg L^{-1}, V is the volume of the dye solution taken in liter and w is the weight of the nanorod (adsorbent) in gram.

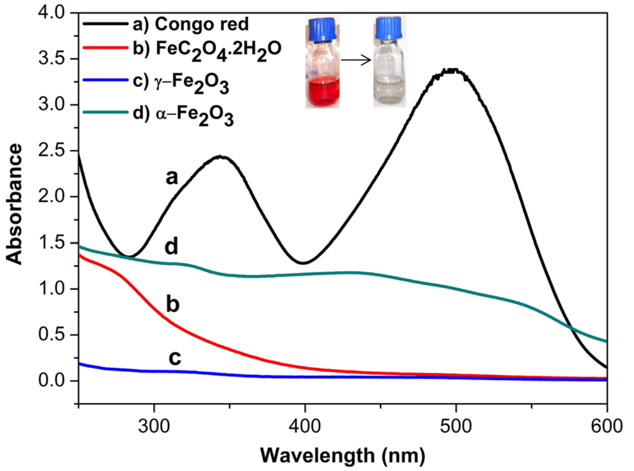

Fig. 1 UV–vis absorption spectra of (*a*) initial CR with a concentration of 100 mg L^{-1} and solutions (20 mL) after treated with 0.05 g of (*b*) $FeC_2O_4 \cdot \mathbf{2H_2}O$, (*c*) γ-$Fe_2O_3$ and (*d*) α-Fe_2O_3 for 30 min

Results and discussion

Surface morphology

Figure 2 shows the SEM micrographs of as synthesized $FeC_2O_4 \cdot 2H_2O$ nanorod, γ-Fe_2O_3 nanorod and α-Fe_2O_3 nanorod. Figure 2a SEM micrograph suggests that the obtained $FeC_2O_4 \cdot 2H_2O$ nanostructure exhibits the morphology of the nanorod with the diameter of about 100–200 nm and the length up to micrometers. Moreover, the surface of the $FeC_2O_4 \cdot 2H_2O$ nanorods seems smooth, and no defects can be observed. When the $FeC_2O_4 \cdot 2H_2O$ nanorods were annealed in air at 300 °C in moist condition, γ-Fe_2O_3 nanorods were fabricated. Figure 2b shows the SEM image of the as-synthesized γ-Fe_2O_3 nanorods. It can be seen that the as-synthesized γ-Fe_2O_3 nanorods retain the morphology of the $FeC_2O_4 \cdot 2H_2O$ nanorods. Similarly, when the $FeC_2O_4 \cdot 2H_2O$ nanorods were annealed in air at 550 °C, α-Fe_2O_3 nanorods were fabricated. Figure 2c shows the SEM image of the as-synthesized α-Fe_2O_3 nanorods. It can also be seen that the as-synthesized α-Fe_2O_3 nanorods retain the morphology of the $FeC_2O_4 \cdot 2H_2O$ nanorods. Figure 2d shows the EDX analysis of as-synthesized γ-Fe_2O_3 nanorods, in which presence of Fe and O is indicated.

A typical profile of TEM images of γ-Fe_2O_3 is shown in Figure 3a and b, which gives further evidence of the formation of high-yield aligned nanorods. A typical TEM image of a single γ-Fe_2O_3 nanorod is given in Fig. 3c, which gives the average diameter of the rod is around 100 nm. The SAED pattern taken from the same single nanorod (given in Fig. 3d) shows sharp bright rings which indicates it is the polycrystalline spinel structure.

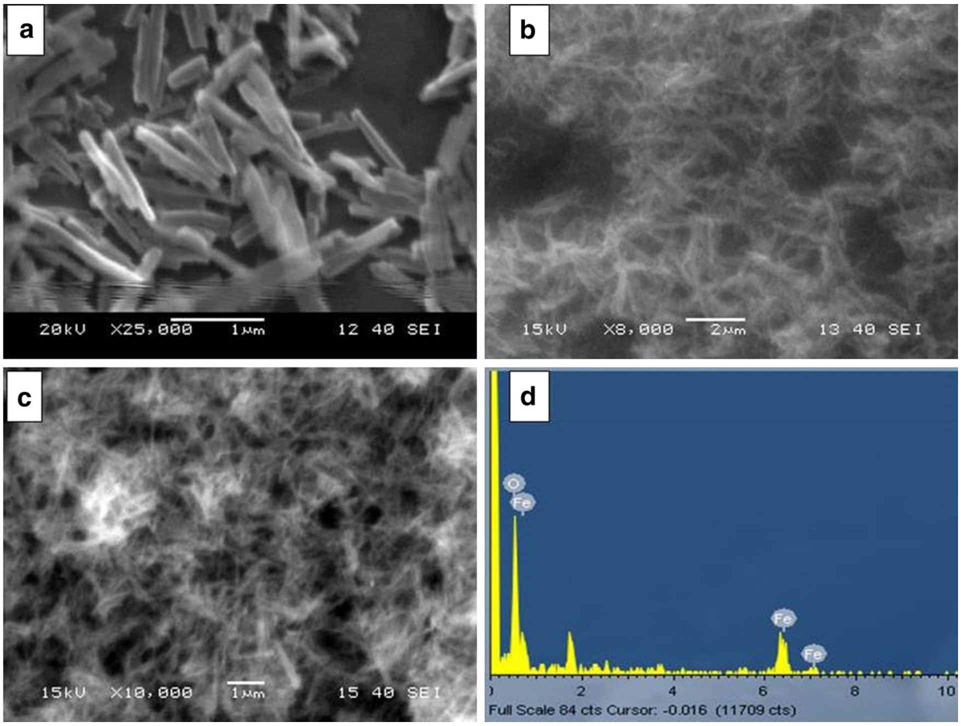

Fig. 2 SEM micrographs of **a** $FeC_2O_4 \cdot 2H_2O$ nanorod, **b** γ-Fe_2O_3 nanorod, **c** α-Fe_2O_3 and **d** EDX of γ-Fe_2O_3 nanorod

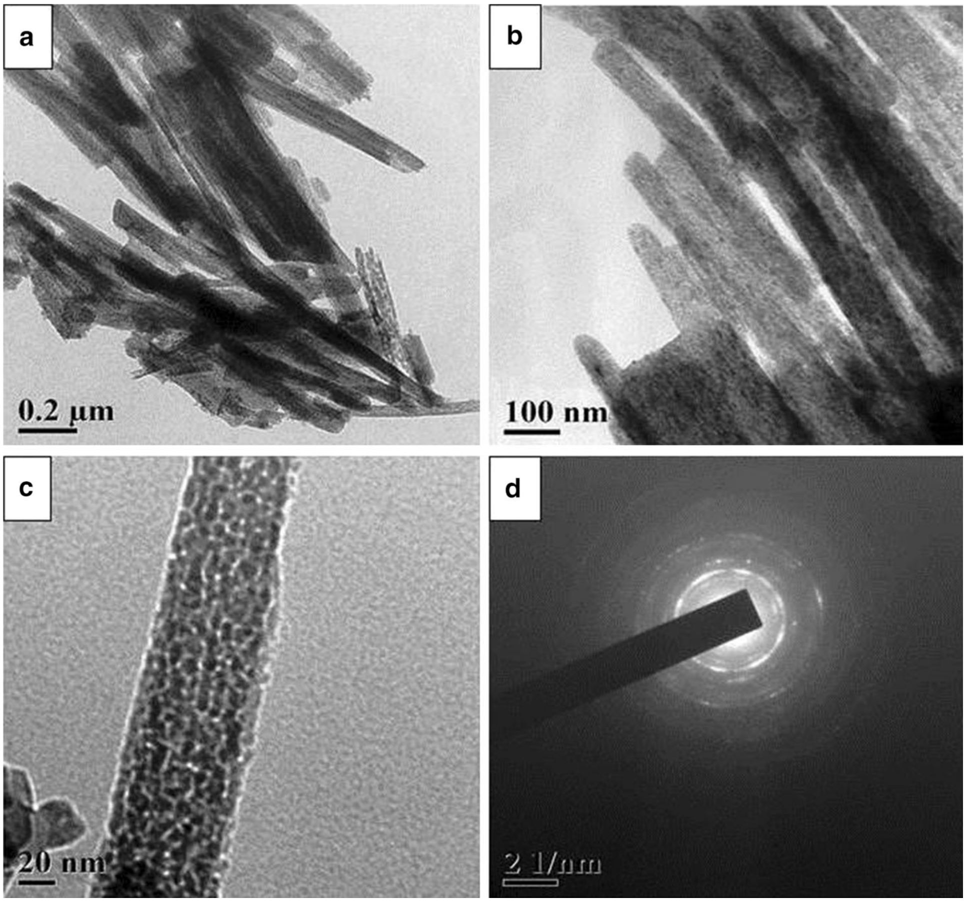

Fig. 3 **a**–**c** TEM images and **d** SAED pattern of γ-Fe_2O_3 nanorod

X-ray diffraction analysis

The formation and phase analysis of the prepared nanomaterials was studied by XRD using Cu Kα radiation. Figure 4 shows the XRD patterns of as synthesised $FeC_2O_4{\cdot}2H_2O$ nanorod, γ-Fe_2O_3 nanorod and α-Fe_2O_3 nanorod. Figure 4a is the XRD pattern of $FeC_2O_4{\cdot}2H_2O$ and contains the characteristics peaks and can be index to orthorhombic crystal structure according to JCPDS No: 22-0635. Figure 4b contains the characteristics peaks of γ-Fe_2O_3 and can be index to cubic crystal structure according to JCPDS No: 39-1346. The XRD pattern of Fig. 4c contains the characteristics peaks of α-Fe_2O_3 and can be index to rhombohedral according to JCPDS No: 79-0007. In Fig. 4b, it is observed that along with peaks of γ-Fe_2O_3, some additional peaks are present (star marked). These are due to presence of small amount of α-Fe_2O_3 in the sample. The X-ray diffractograms reveal the well crystalline nature of the compounds. The broadening of the peaks also indicates the decrease in the diameter and an increase in the surface-to-volume ratio of the compounds. Crystallite size and the lattice strain of the prepared samples are calculated from the X-ray diffractograms. From the well-known Scherrer formula, the average crystallite size, L, is:

$$L = \frac{K\lambda}{\beta\cos\theta} \tag{2}$$

where λ is the X-ray wavelength, θ is the diffraction angle, β is the line broadening at half the maximum intensity (FWHM) in radians resulting from small crystallite size and K is a constant approximately equal to unity and related to crystallite shape. The crystallite size and lattice strain of ferrous oxalate were found to be 22.6 nm and 1.196 %, respectively. When it is heated to 300 °C form γ-Fe_2O_3, its crystallite size increased to 29.4 nm while lattice strain decreased to 0.5. Similarly, when the sample further heated to higher temperature to form α-Fe_2O_3, its crystallite size still increases and lattice strain decreases. This phenomenon is also observed in the XRD patterns that for ferrous oxalate consists broadened peaks and γ-Fe_2O_3 consists less broadened peaks while α-Fe_2O_3 contains comparatively sharp peaks. As the lattice strain of α-Fe_2O_3 is least, it is the most stable form among the three samples. The unit-cell dimension of the synthesized samples was measured to determine the crystal structure and given in Table 1.

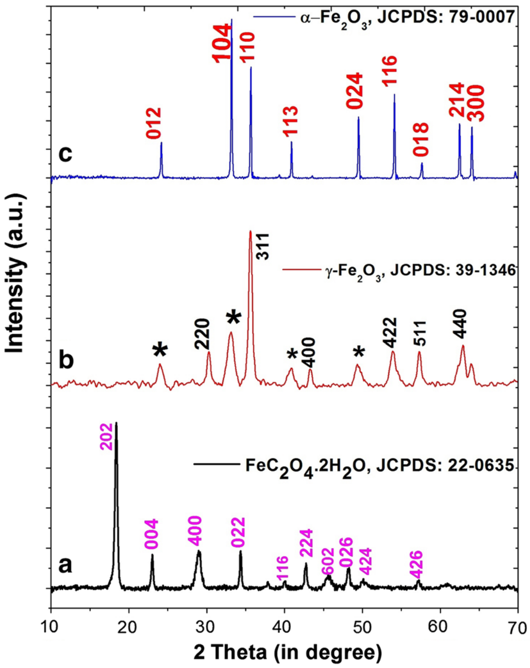

Fig. 4 XRD patterns of (*a*) $FeC_2O_4{\cdot}2H_2O$ nanorod, (*b*) γ-Fe_2O_3 nanorod and (*c*) α-Fe_2O_3 nanorod

FTIR study

To further confirm the formation and transformation from $FeC_2O_4{\cdot}2H_2O$ to γ-Fe_2O_3 and α-Fe_2O_3, FTIR analysis was performed. In Fig. 5a pattern, the peaks at 3,358, 1,631, 1,315 and 496 cm^{-1} are attributed to O–H, C=O, C–O and Fe–O functional groups, respectively, indicating the formation of $FeC_2O_4{\cdot}2H_2O$. In Fig. 5b pattern, the peak at 632 cm^{-1} is due to Fe–O, which is characteristic peak of maghemite and at 1,637 cm^{-1} is due to presence of water of crystallization in the sample. In Fig. 5c pattern, the peaks at 617 cm^{-1} is due to longitudinal adsorption (A_u) and at 572 and 490 cm^{-1} are due to transverse adsorption (E_u) of Fe–O vibrational mode of hematite.

UV–vis diffuse reflectance spectra

The optical characterization of the prepared nanomaterials such as electronic transition and band energy gap was done by UV–visible absorbance spectra. The spectral absorption coefficient, α, is defined as,

Table 1 Crystallographic information of the prepared nanorods

Sample	Crystal structure	Lattice parameters (°A)	Crystallite size (nm)	Lattice strain (%)
$FeC_2O_4{\cdot}2H_2O$	Orthorhombic	$a = 12.26$, $b = 5.57$, $c = 15.48$	22.6	1.196
γ-Fe_2O_3	Cubic	$a = 8.3515$	29.4	0.5
α-Fe_2O_3	Rhombohedral	$a = b$=5.0285, $c = 13.736$	39.1	0.433

$$\alpha(\lambda) = \frac{4\pi k(\lambda)}{\lambda} \tag{3}$$

where (λ) is the spectral extinction coefficient obtained from the absorption curve and λ is the wavelength. Figure 6 shows the visible and near-UV diffuse reflectance spectra of the ferrous oxalate and the two iron oxides. From the spectrum of ferrous oxalate, it is observed that there is an intense band around 210 nm and an asymmetric band at 400 nm. The intense band corresponds to the charge transfer band and the less intense band arises due to $^5T_{2g} \rightarrow {}^5E_g$. In case of γ-Fe_2O_3 spectrum, it is observed that absorption peaks at 302, 357 and 421 nm correspond to $^6A_1 \rightarrow {}^4T_1$, $^6A_1 \rightarrow {}^4E$ and $2(^6A_1) \rightarrow 2(^4T_1)$ ligand-free transition of Fe^{+3}, respectively, while the peak at 512 nm corresponds to finger print region of the band edge of maghemite (Sherman and Waite 1985). From the spectrum of α-Fe_2O_3, it is observed that absorption peaks at 339, 355, 484 and 537 nm. The peaks at 355 and 484 nm correspond to $^6A_1 \rightarrow {}^4E$ and $2(^6A_1) \rightarrow 2(^4T_1)$ ligand field transition of Fe^{3+}, respectively. Again, the peak at 537 nm corresponds to finger print region of the band edge of hematite. This experiment further confirms the formation of pure α-Fe_2O_3 (Zhu et al. 2012a, b).The optical band gap E_g can be experimentally obtained from absorption coefficient measurements using Tauc's formula (Miller et al. 2004):

$$(\alpha h\nu) = A(h\nu - E_g)^n \tag{4}$$

where α is the absorption coefficient, A is a constant and n is equal to 1/2 for allowed direct transitions and 2 for allowed indirect transitions. The band gap value, E_g, of the prepared nanorods was evaluated by extrapolating the linear portion of the curve. It is found that the energy band gaps of $FeC_2O_4{\cdot}2H_2O$, γ-Fe_2O_3 and α-Fe_2O_3 are 2.24, 1.95 and 2.04 eV, respectively. So, it may be considered that all the prepared nanorods possess semiconducting properties with narrow band gap.

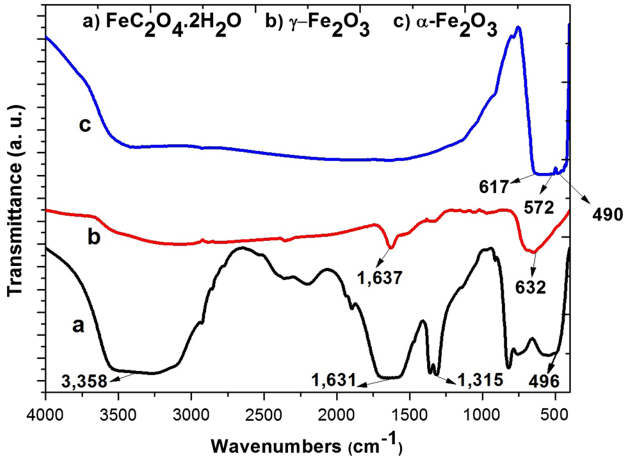

Fig. 5 FTIR spectra of (*a*) $FeC_2O_4{\cdot}2H_2O$ nanorod, (*b*) γ-Fe_2O_3 nanorod and (*c*) α-Fe_2O_3 nanorod

N_2 adsorption–desorption isotherm

The surface area and porosity nature of the prepared nanorods was carried out by N_2 adsorption–desorption isotherm

Fig. 6 **a** Visible and near-ultraviolet absorption spectra of $FeC_2O_4{\cdot}2H_2O$, γ-Fe_2O_3 and α-Fe_2O_3 and Tauc plots of **b** $FeC_2O_4{\cdot}2H_2O$, **c** γ-Fe_2O_3 and **d** α-Fe_2O_3

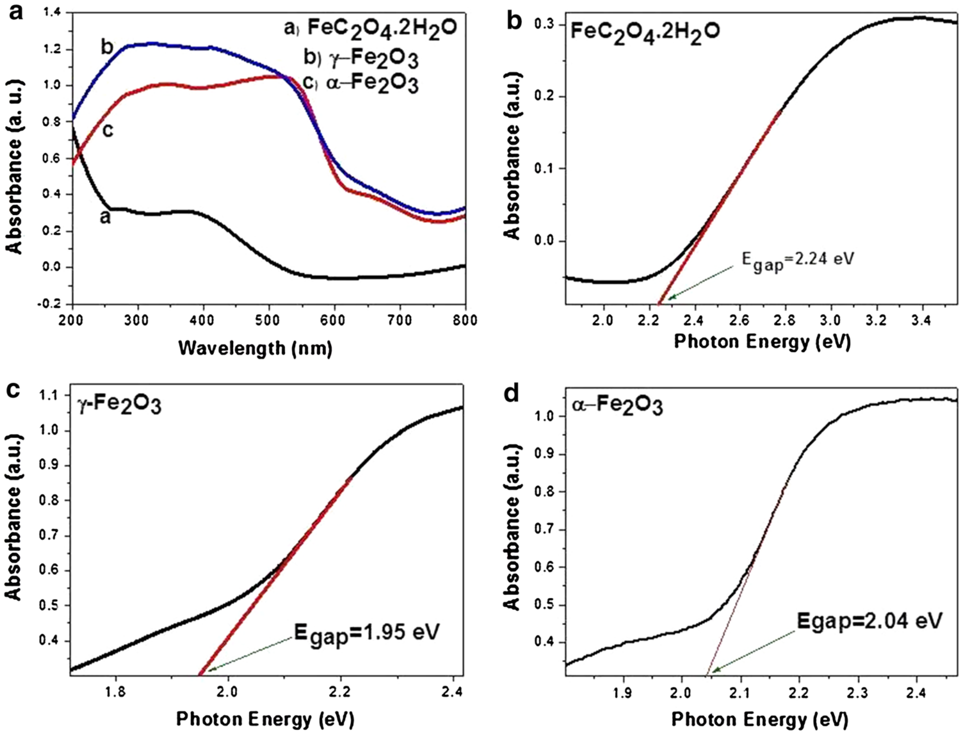

technique. The adsorption–desorption isotherm and pore size distribution are shown in Fig. 7. From Fig. 7a, it is observed that the BET and Langmuir surface areas of the prepared ferrous oxalate were found to be 27.550 and 24.945 $m^2\ g^{-1}$. From the BJH graph, the pore volume and average pore diameter were found to be 0.0857 mL g and 7 nm, respectively. From Fig. 7b, the BET and Langmuir surface areas of γ-Fe_2O_3 were found to be 129.74 and 107.35 $m^2\ g^{-1}$, and from the BJH graph, the pore volume and average pore diameter were found to be 0.1744 mL g^{-1} and 6 nm, respectively. Similarly, from Fig. 7c, the BET and Langmuir surface areas of α-Fe_2O_3 were found to be 22.785 and 20.575 $m^2\ g^{-1}$, and from the BJH graph, the pore volume and average pore diameter were found to be 0.03445 mL g^{-1} and 9 nm, respectively. From the above discussion, it is observed that the surface area of γ-Fe_2O_3 is highest among the prepared nanorods.

Effect of operational factors on adsorption

Effect of adsorbent dose

Adsorbent dosage is one of the most important parameter that has been considered to determine the optimum condition for the performance of adsorption. Essentially, insufficient dosage or overdosing would result in the poor performance in adsorption. Therefore, it is significant to determine the optimum dosage in order to minimize the dosing cost and sludge formation and also to obtain the optimum performance in treatment. The effect of adsorbent doses on the removal of CR using $FeC_2O_4{\cdot}2H_2O$, α-Fe_2O_3 and γ-Fe_2O_3 nanorods maintaining pH 7.6 (pH at normal condition) for 20 mL of 100 mg L^{-1} CR solution and 30 min contact time is represented in Fig. 8a. It is observed there is a continuous removal of CR with increase in adsorbent dose up to 0.05 g. This may be due to an increase in number of active sites of the adsorbent material with increasing amount of the adsorbent. Further increase in the amount of the adsorbent does not bring any considerable change in the adsorption, i.e., approximately straight line after 0.05 g thus 0.05 g was chosen as the optimum amount for all studies of the adsorbents. The highest percentage of removal obtained for γ-Fe_2O_3 nanorod among the three adsorbents.

Effect of contact time

The time of contact of adsorption is another parameter for adsorption. It is helpful in understanding the amount of dye adsorbed at various time intervals by a fixed amount of the adsorbent. In this section, 0.05 g of each adsorbents used in 20 mL 100 mg L^{-1} of CR solution maintaining pH 7.6, with varying time from 0 to 60 min. From Fig. 8b, it is found that there is a consistent increase in percentage of removal up to 30 min and the adsorption equilibrium is attained after 30 min of contact time. This is due to the rate of adsorption decreased, and a saturation stage was attained due to the accumulation of the adsorption sites by the dye ions. The highest removal of

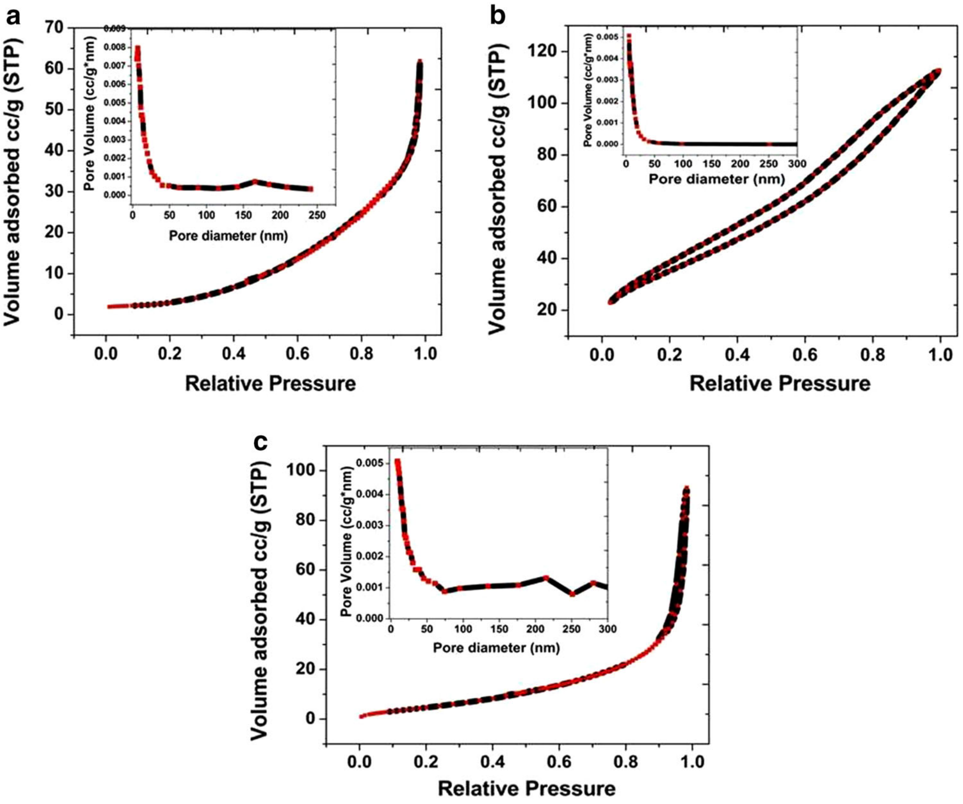

Fig. 7 BET isotherm and BJH isotherm (*inset*) of **a** ferrous oxalate, **b** γ-Fe_2O_3 and **c** α-Fe_2O_3 nanorods

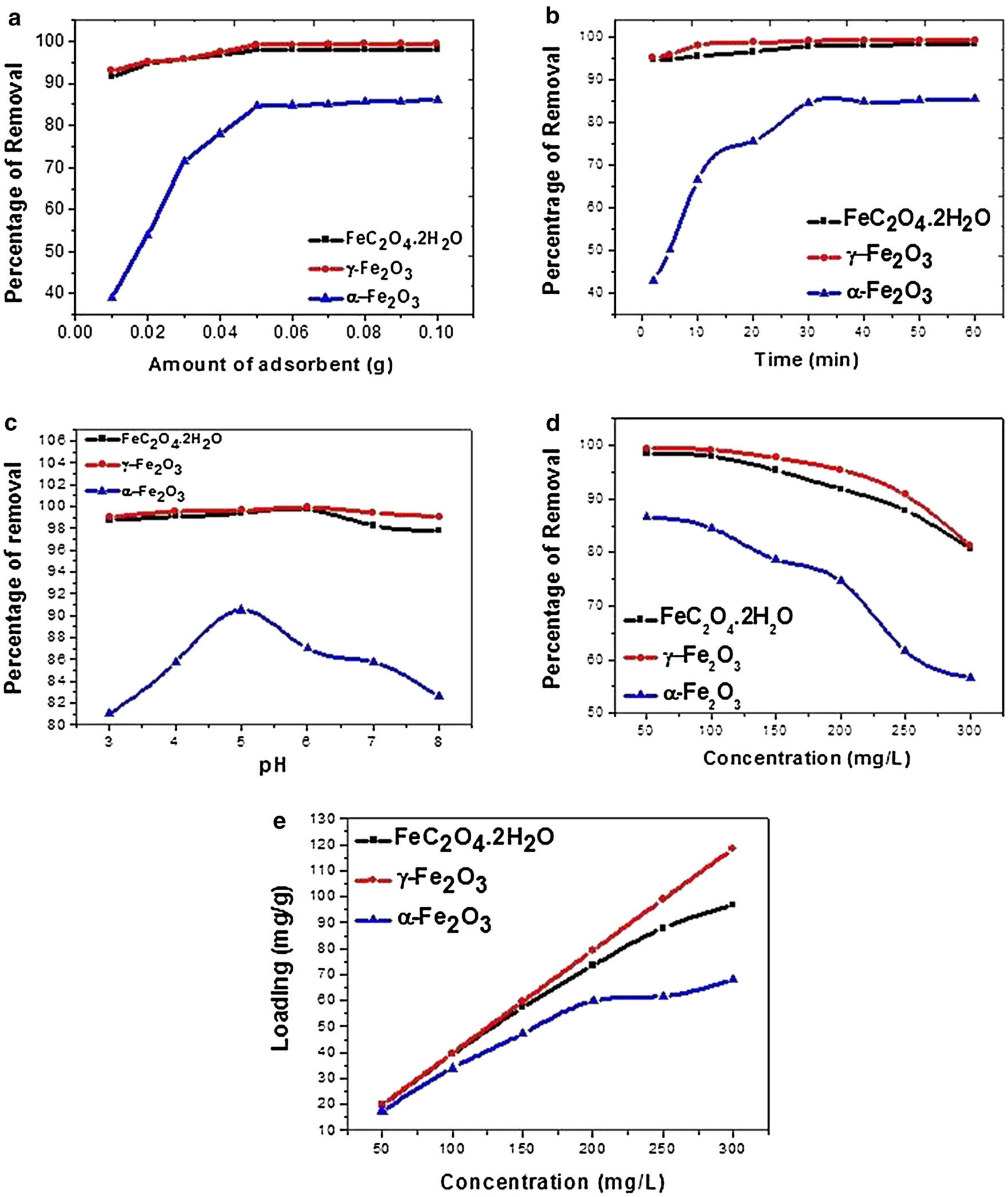

Fig. 8 Effect of **a** amount of adsorbent (dose), **b** time, **c** pH and **d** concentration on removal of CR by: *square* $FeC_2O_4{\cdot}2H_2O$, *circle* γ-Fe_2O_3 and *triangle* α-Fe_2O_3 nanorods and **e** effect of initial dye concentration on adsorption capacity for the removal of CR

CR is found to be 97.97 % for $FeC_2O_4{\cdot}2H_2O$, 99.24 % for γ-Fe_2O_3 and 84.62 % for α-Fe_2O_3 for 30 min contact time. Agitation time of 30 min was selected for further works.

Effect of pH on CR solution

To investigate the effect of pH on the adsorption of CR dye, the pH range 3–8 was chosen. The pH of the test solutions was adjusted by using HCl and NaOH solutions. An amount of 0.05 g of each adsorbents were used in 20 mL of 100 mg L^{-1} CR solution of each pH with 30 min agitation time. From Fig. 8c, it is found that for $FeC_2O_4{\cdot}2H_2O$ and γ-Fe_2O_3, there is no significant change in the percentage adsorption by increasing pH from 3 to 6 and reached maximum at pH 6 and then slightly decreased at higher pH in case of $FeC_2O_4{\cdot}2H_2O$. For α-Fe_2O_3, the maximum percentage of removal occurs at pH 5 and then decreases. This is due to at higher pH, the adsorbents surface become negatively charged. Therefore the adsorbents did not favour the adsorption of negatively charged CR dye due to electrostatic repulsion (Afkhami and Moosavi 2010).

Effect of initial dye concentration on adsorption

The adsorption is greatly influenced by the concentration of the solution, as the adsorptive reactions are directly proportional to the concentration of the solute (Mittal et al. 2009). It this section, 0.05 g of each adsorbent used each 20 mL of CR solution (natural pH) with concentration ranging from 50 to 300 mg L^{-1} and the agitation time was kept 30 min. It is found that with the increase in initial dye concentration, percentage adsorption decreases (Fig. 8d) while the equilibrium adsorption capacity of the adsorbent for CR increases with increasing initial dye concentration, i.e., the more concentrated the dye solution, the higher the adsorption capacity (Fig. 8e). This is probably due to a high driving force for mass transfer in high dye concentration.

Adsorption isotherm

To determine equilibrium relationship of amount adsorbed by a unit weight of adsorbent (q_e) with the concentration of adsorbent remaining in the medium at equilibrium (C_e), studies of various adsorption isotherm models are required. There is various type of adsorption models developed such as Freundlich, Langmuir, Tempkin and D–R isothermal models. (Mittal et al. 2009). The most common models such as Freundlich and Langmuir equations are used to investigation of this study.

Langmuir isotherm

The Langmuir isotherm model assumes monolayer coverage of adsorbate on a homogeneous adsorbent surface. This model does not consider surface heterogeneity of the sorbent. It assumes adsorption will take place only at specific site on the adsorbent (Chatterjee et al. 2009). The Langmuir equation is given as:

$$\frac{q_e a_L}{K_L} = \frac{K_L C_e}{(1 + K_L C_e)} \tag{5}$$

The linear form of the Langmuir isotherm is:

$$\frac{C_e}{q_e} = \frac{1}{K_L q_{\max}} + C_e/q_{\max} \tag{6}$$

where a_L (L mg^{-1}) and K_L (L g^{-1}) are the Langmuir constants, $q_{\max}(=K_L/a_L)$ is the maximum adsorption capacity corresponding to complete monolayer coverage (mg g^{-1}), which depends upon the number of adsorption sites (Rahimi et al. 2011). The values of $q_{\max}$ and K_L are calculated from the slopes and intercepts of the straight lines of plot of C_e/q_e versus C_e.

Freundlich isotherm

The Freundlich isotherm model is an empirical equation that describes the surface heterogeneity of the sorbent. It considers multilayer adsorption with a heterogeneous energetic distribution of active sites, accompanied by interactions between adsorbed molecules (Namasivayam and Kavitha 2002). The Freundlich isotherm equation is given as:

$$q_e = K_F C_e^{1/n} \tag{7}$$

The linear form of the Freundlich isotherm is:

$$\ln q_e = \ln K_F + {}^{1}\!/_{n} \ln C_e \tag{8}$$

where C_e is the equilibrium concentration (mg L^{-1}), q_e is the amount adsorbed at equilibrium (mg g^{-1}) and K_F and n are Freundlich constants, related to the extent of the adsorption and the degree of nonlinearity between solution concentration and adsorption, respectively. K_F and (1/n) can be determined from the linear plot of ln q_e versus ln C_e.

The essential characteristics of Langmuir isotherm can be expressed by a dimensionless constant called equilibrium parameter (R_L) that is defined by the following equation (Chatterjee et al. 2009; Afkhami et al. 2009):

$$R_L = \frac{1}{1 + a_L C_0} \tag{9}$$

where a_L and C_0 are the parameters as defined previously. The value of R_L calculated from the above expression. The nature of the adsorption process to be either unfavorable ($R_L > 1$), linear ($R_L = 1$), favorable ($0 < R_L < 1$) or irreversible ($R_L = 0$) (Lian et al. 2009). Here, R_L values obtained are listed in Table 2. The linear Langmuir and Freundlich plots for the adsorption of CR onto the three

Table 2 Adsorption isotherm constants for adsorption of CR

Adsorbent	a_L (L mg^{-1})	K_L (L g^{-1})	$q_{\max}$ (mg g^{-1})	r_L^2	R_L
Langmuir					
$FeC_2O_4{\cdot}2H_2O$	0.0022	0.224	103.09	0.996	0.82
γ-Fe_2O_3	0.0012	0.267	232.56	0.998	0.89
α-Fe_2O_3	0.00064	0.048	78.13	0.995	0.999

Adsorbent	K_F	1/n	r_F^2
Freundlich			
$FeC_2O_4{\cdot}2H_2O$	26.5	0.3493	0.957
γ-Fe_2O_3	46.42	0.7434	0.993
α-Fe_2O_3	8.99	0.442	0.914

Fig. 9 Linearization of Langmuir plots of **a** $FeC_2O_4 \cdot 2H_2O$, **b** γ-Fe_2O_3 and **c** α-Fe_2O_3 and Freundlich plots of **d** $FeC_2O_4 \cdot 2H_2O$, **e** γ-Fe_2O_3 and **f** α-Fe_2O_3 for the adsorption of CR

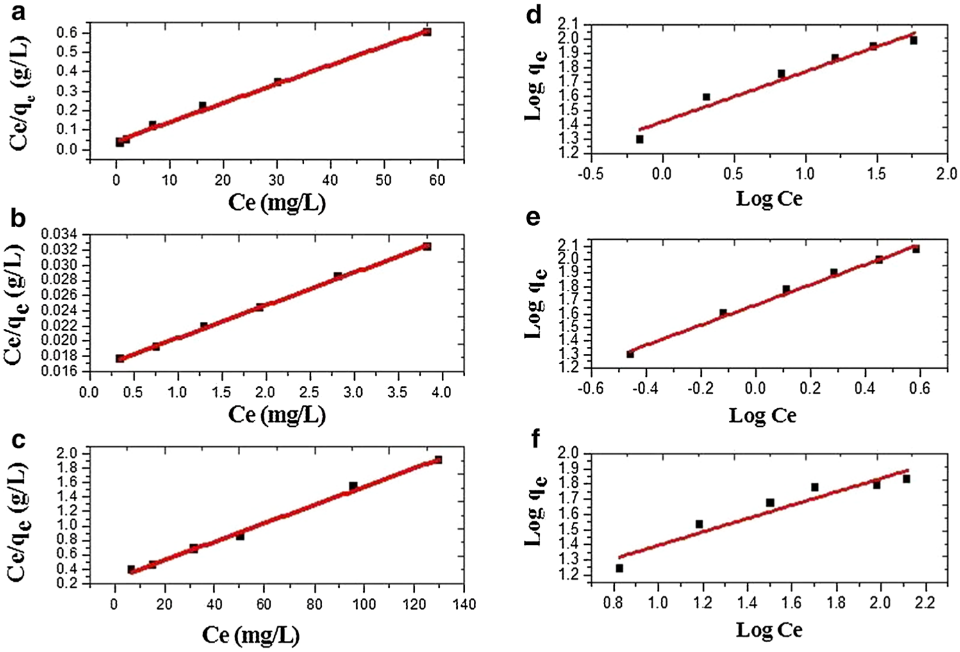

nanorod adsorbents are obtained by plotting C_e/q_e versus C_e and ln q_e versus ln C_e, respectively (given in Fig. 9). The isotherm constants and correlation coefficients were calculated and listed in Table 2. By comparing the correlation coefficients r_L^2, it can be deduced that the experimental equilibrium adsorption data are well described by both the Langmuir and Freundlich models, but the Langmuir model is more suitable. The maximum adsorption capacity of 103.09, 232.56 and 78.13 mg g^{-1} was found for $FeC_2O_4 \cdot 2H_2O$, γ-Fe_2O_3 and α-Fe_2O_3, respectively. For Freundlich isotherm model, the n value between 1 and 10 indicates beneficial adsorption (Chen and Zhao 2009). Comparing the q_{max} values of the different adsorbents, it is observed that γ-Fe_2O_3 nanorod has higher adsorption capacity than $FeC_2O_4 \cdot 2H_2O$ and α-Fe_2O_3 nanorods.

Adsorption kinetics

In order to investigate the adsorption processes of CR on the adsorbents, pseudo-second-order kinetic is used. The pseudo-second-order model is represented as (Ho and McKay 1999):

$$\frac{t}{q} = \frac{1}{k_2 q_e^2} + \frac{t}{q_e} \quad (10)$$

And the initial adsorption rate, h (mg g^{-1} min^{-1}), as $t \to 0$ can be defined as:

$$h = k_2 q_e^2 \quad (11)$$

The initial adsorption rate (h), the equilibrium adsorption capacity (q_e) and the second-order constants k_2 (g^{-1} mg min) can be determined experimentally from the slope and intercept of plot of t/q versus t. The best-fit values of h, q_e and k_2 along with correlation coefficients of the pseudo-second-order model for the three adsorbents are shown in Table 3, and the pseudo-second-order plots of $FeC_2O_4 \cdot 2H_2O$, γ-Fe_2O_3 and α-Fe_2O_3 are given in Fig. 10. The values of predicted equilibrium adsorption capacities (q_e) showed good agreement with the experimental equilibrium uptake values. Similarly, correlation coefficients are always greater than 0.99, which also explains the good fit of the model.

The maximum adsorption capacity (q_{max}) for the adsorption of CR on γ-Fe_2O_3 nanorod compared to other adsorbents is listed in Table 4. It is observed that the prepared γ-Fe_2O_3 nanorod is an efficient adsorbent for adsorption of CR from aqueous solution.

Table 3 Second-order kinetic parameters for the removal of CR

Adsorbents	K_2 (g mg^{-1} min^{-1})	q_e (mg g^{-1})	q_e (mg g^{-1}) (experimental)	r^2
$FeC_2O_4 \cdot 2H_2O$	0.0999	39.53	39.19	1
γ-Fe_2O_3	0.0933	40	39.7	1
α-Fe_2O_3	0.00891	36.23	34.23	0.9986

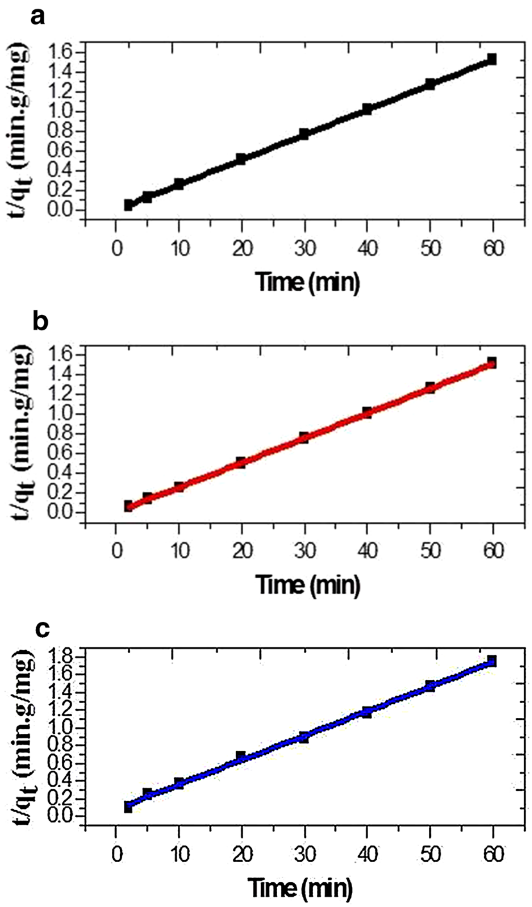

Fig. 10 Pseudo-second-order kinetic plots of **a** $FeC_2O_4{\cdot}2H_2O$, **b** γ-Fe_2O_3 and **c** α-Fe_2O_3

Table 4 Comparison of CR adsorption capacities of various adsorbents

Types of adsorbent	q_{max} (mg g^{-1})	References
Chitosan/montmorillonite nanocomposite	54.52	Wang and Wang (2007)
Montmorillonite	12.70	Wang and Wang (2007)
Mesoporous activated carbons	189	Lorenc-Grabowska and Gryglewicz (2007)
γ-Fe_2O_3 nanoparticles	208.33	Afkhami and Moosavi (2010)
Chitosan Bead	162.32	Chatterjee et al. (2009)
γ-Fe_2O_3 nanorod	232.56	Present work
$FeC_2O_4{\cdot}2H_2O$ nanorod	103.09	Present work
α-Fe_2O_3 nanorod	78.13	Present work

Conclusion

In this present study, we have synthesized ferrous oxalate nanorods by a modified co-precipitation by using ferrous sulfate and oxalic acid as starting material and CTAB as surfactant. Then the obtained nanoparticles are calcined at higher temperature to form γ-Fe_2O_3 and α-Fe_2O_3 nanorods. SEM images indicate the formation of rod-shaped nanoparticles with diameter around 100–200 nm and length up to micrometers. The formation of the phase, crystallite sites, lattice parameters, lattice strains and crystal structure are determined by XRD study. It is found that the crystallite sizes are 22.6, 29.4 and 39.1 nm, for $FeC_2O_4{\cdot}2H_2O$, γ-Fe_2O_3 and α-Fe_2O_3 nanorods, respectively. Further confirmation of formation is done by FTIR using the different vibrational peaks. The electronic transition of Fe^{+2} ion for $FeC_2O_4{\cdot}2H_2O$ and Fe^{+3} for γ-Fe_2O3 and α-Fe_2O_3 was studied by UV–vis DRS spectra. From this spectra, energy band gap was calculated and found to be 2.24, 1.95 and 2.04 eV for $FeC_2O_4{\cdot}2H_2O$, γ-Fe_2O_3 and α-Fe_2O_3, respectively, which confirms that all the three nanorods possess semiconducting properties with narrow band gap. Then, the three prepared 1-dimensional nanomaterials such as ferrous oxalate nanorod, maghemite (γ-Fe_2O_3) nanorod and hematite (α-Fe_2O_3) nanorod were used as adsorbent for removal of carcinogenic organic dye such as CR from aqueous solution. From the adsorption study, it is found that the maximum adsorption capacities of the adsorbents are 103.09, 232.56 and 78.13 mg g^{-1} for $FeC_2O_4{\cdot}2H_2O$, γ-Fe_2O_3 and α-Fe_2O_3 nanorods, respectively. This result indicates that among the three prepared 1-dimensional nanomaterials, γ-Fe_2O_3 nanorods are the most effective adsorbent for the adsorption of CR from aqueous solution.

Acknowledgments The authors would like to acknowledge National Institute of Technology Rourkela, Odisha, India for providing the research funding and facilities to carry out this research work.

References

Afkhami A, Moosavi R (2010) Adsorptive removal of Congo red, a carcinogenic textile dye, from aqueous solutions by maghemite nanoparticles. J Hazard Mater 174:398–403

Afkhami A, Saber-Tehran M, Bagheri H (2009) Modified maghemite nanoparticles as an efficient adsorbent for removing some cationic dyes from aqueous solution. Desalination 263:240–248

Bhattacharyya KG, Sharma A (2004) Azadirachta indica leaf powder as an effective biosorbent for dyes: a case study with aqueous Congo red solutions. J Environ Manage 71:217–229

Binupriya AR, Sathishkumar M, Swaminathan K, Ku CS, Yun SE (2008) Comparative studies on removal of Congo red by native and modified mycelial pellets of Trametes versicolor in various reactor modes. Bioresour Technol 99:1080–1088

Chakraborty S, Purkait MK, Dasgupta S, De S, Basu JK (2003) Nanofiltration of textile plant effluent for color removal and reduction in COD. Sep Purif Technol 31:141–151

Chan LS, Cheung WH, Allen SJ, McKay G (2009) Separation of acid-dyes mixture by bamboo derived active carbon. Sep Purif Technol 67:166–172

Chatterjee S, Lee MW, Woo SH (2009) Enhanced adsorption of congo red from aqueous solutions by chitosan hydrogel beads impregnated with cetyl trimethyl ammonium bromide. Bioresour Technol 100:2803–2809

Chatterjee S, Lee MW, Woo SH (2010) Adsorption of congo red by chitosan hydrogel beads impregnated with carbon nanotubes. Bioresour Technol 101:1800–1806

Chen H, Zhao J (2009) Adsorption study for removal of Congo red anionic dye using organo-attapulgite. Adsorption 15:381–389

Chowdhury AK, Sarkar AD, Bandyopadhyay A (2009) Rice Husk Ash as a Low Cost Adsorbent for the Removal of Methylene Blue and Congo red in Aqueous Phases. Clean –Soil Air. Water 37(7):581–591

Dawood S, Sen TK (2012) Removal of anionic dye Congo red from aqueous solution by raw pine and acid-treated pine cone powder as adsorbent: equilibrium, thermodynamic, kinetics, mechanism and process design. Water Res 46:1933–1946

Dizge N, Aydiner C, Demirbas E, Kobya M, Kara S (2008) Adsorption of reactive dyes from aqueous solutions by fly ash: kinetic and equilibrium studies. J Hazard Mater 150:737–746

Fu Y, Viraraghavan T (2002) Removal of Congo red from an aqueous solution by fungus Aspergillus niger. Adv Environ Res 7:239–247

Ge F, Ye H, Li MM, Zhao BX (2012) Efficient removal of cationic dyes from aqueous solution by polymer-modified magnetic nanoparticles. Chem Eng J 198–199:11–17

Haider S, Bukhari N, Park SY, Iqbal Y, Al-Masry WA (2011) Adsorption of bromo-phenol blue from an aqueous solution onto thermally modified granular charcoal. Chem Eng Res Des 89:23–28

Ho YS, McKay G (1999) Pseudo-second order model for sorption processes. Process Biochem 34:451–465

Hu J, Song Z, Chen L, Yang H, Li J, Richards R (2010a) Adsorption Properties of MgO(111) Nanoplates for the Dye Pollutants from Wastewater. J Chem Eng Data 55:3742–3748

Hu Z, Chen H, Ji F, Yuan S (2010b) Removal of Congo red from aqueous solution by cattail root. J Hazard Mater 173:292–297

Irama M, Guo C, Guan Y, Ishfaq A, Liu H (2010) Adsorption and magnetic removal of neutral red dye from aqueous solution using Fe3O4 hollow nanospheres. J Hazard Mater 181:1039–1050

Jain R, Sikarwar S (2008) Removal of hazardous dye congo red from waste material. J Hazard Mater 152:942–948

Khadhraoui M, Trabelsi H, Ksibi M, Bouguerra S, Elleuch B (2009) Discoloration and detoxification of Congo red dye solution by means of ozone treatment for a possible water reuse. J Hazard Mater 161:974–981

Kumar J, Bansal A (2012) Photodegradation of amaranth in aqueous solution catalyzed by immobilized nanoparticles of titanium dioxide. Int J Environ Sci Technol 9(3):479–484. doi:10.1007/s13762-012-0064-4

Lian L, Guo L, Guo C (2009) Adsorption of Congo red from aqueous solutions onto Ca-bentonite. J Hazard Mater 161:126–131

Lorenc-Grabowska E, Gryglewicz G (2007) Adsorption characteristics of Congo red on coal-based mesoporous activated carbon. Dyes Pigm 74:34–40

Lucas MS, Peres JA (2006) Decolorization of the azo dye Reactive Black 5 by Fenton and photo-Fenton oxidation. Dyes Pigments 71:236–244

Marechal ML, Slokar YM, Taufer T (1997) Decolouration of chlorotriazine reactive azo dyes with H_2O_2/UV. Dyes Pigments 33:281–298

Miller EL, Paluselli D, Marsen B, Rocheleau RE (2004) Low-temperature reactively sputtered iron oxide for thin film devices. Thin Solid Films 466:307–313

Mittal A, Mittal J, Malviya A, Gupta VK (2009) Adsorptive removal of hazardous anionic dye ‘‘Congo red’’ from wastewater using waste materials and recovery by desorption. J Colloid Interface Sci 340:16–26

Namasivayam C, Kavitha D (2002) Removal of Congo red from water by adsorption onto activated carbon prepared from coir pith, an agricultural solid waste. Dyes Pigm 54:47–58

Nethaji S, Sivasamy A, Mandal AB (2012) Adsorption isotherms, Kinetics and mechanisms for the adsorption of cationic and anionic dyes onto carbonaceous particles prepared from Juglans regia shell biomass. Int J Environ Sci Technol 10(2):231–242

Panda GC, Das SK, Guha AK (2009) Jute stick powder as a potential biomass for the removal of congo red and rhodamine B from their aqueous solution. J Hazard Mater 164:374–379

Pavan FA, Dias SLP, Lima EC, Benvenutti EV (2008) Removal of Congo red from aqueous solution by anilinepropylsilica xerogel. Dyes Pigm 76:64–69

Purkait MK, Dasgupta S, De S (2004) Removal of dye from wastewater using micellar-enhanced ultrafiltration and recovery of surfactant. Sep Purif Technol 37:81–92

Purkait MK, Maiti A, Dasgupta S, De S (2007) Removal of congo red using activated carbon and its regeneration. J Hazard Mater 145:287–295

Rahimi R, Kerdari H, Rabbani M, Shafiee M (2011) Synthesis, characterization and adsorbing properties of hollow Zn-Fe_2O_4 nanospheres on removal of congo red from aqueous solution. Desalination 280:412–418

Sachdeva S, Kumar A (2009) Preparation of nonporous composite carbon membrane for separation of Rhodamine B dye. J Membr Sci 329:2–10

Sherman DM, Waite TD (1985) Electronic spectra of Fe^{3+} oxides and oxide hydroxides in the near IR to near UV. Am Mineral 70:1262–1269

Song YL, Li JT, Chen H (2009) Degradation of C.I. Acid red 88 aqueous solution by combination of Fenton’s reagent and ultrasound irradiation. J Chem Technol Biotechnol 84:578–583

Song HJ, Liu L, Jia XH, Min C (2012) Synthesis of multi-walled carbon nanotubes/β-FeOOH nanocomposites with high adsorption capacity. J Nanopart Res 14:1–8

Toor M, Jin B (2012) Adsorption characteristics, isotherm, kinetics, and diffusion of modified natural bentonite for removing diazo dye. Chem Eng J 187:79–88

Vijayakumar G, Dharmendirakumar M, Renganathan S, Sivanesan S, Baskar G, Elango KP (2009) Removal of Congo red fromAqueous Solutions by Perlite. Clean-Soil Air Water 37(4–5):355–364

Wang L, Wang A (2007) Adsorption characteristics of congo red onto the chitosan/montmorillonite nanocomposite. J Hazard Mater 147:979–985

Wang L, Wang A (2008) Adsorption properties of Congo red from aqueous solution onto surfactant-modified montmorillonite. J Hazard Mater 160:173–180

Wang L, Li J, Wang Y, Zhao L, Jiang Q (2012a) Adsorption capability for Congo red on nanocrystalline MFe_2O_4 ($M = Mn$, Fe Co, Ni) spinel ferrites. Chem Eng J 181–182:72–79

Wang L, Wu XL, Xu WH, Huang XJ, Liu JH, Xu AW (2012b) Stable Organic–Inorganic Hybrid of Polyaniline/α-Zirconium Phosphate for Efficient Removal of Organic Pollutants in Water Environment. ACS Appl. Mater. Interfaces 4:2686–2692

Wawrzkiewicz M (2012) Comparison of the efficiency of amberlite IRA 478RF for acid, reactive, and direct dyes removal from aqueous media and wastewaters. Ind Eng Chem Res 51:8069–8078

Wawrzkiewicz M, Hubicki Z (2010) Equilibrium and kinetic studies on the sorption of acidic dye bymacro porous anion exchange. Chem Eng J 157:29–34

Yosef I, Avnir D (2011) Entrapment of dye molecules within submicron silver particles. J Nanopart Res 13:3929–3937

Yu C, Dong X, Guo L, Li J, Qin F, Zhang L, Shi J, Yan D (2008) Template-free preparation of mesoporous Fe_2O_3 and its application as absorbents. J Phys Chem C 112:13378–13382

Zhu M, Wang Y, Meng D, Qin X, Diao G (2012a) Hydrothermal synthesis of hematite nanoparticles and their electrochemical properties. J Phys Chem C 116:16276–16285

Zhu T, Chen JS, Lou XWD (2012b) Highly efficient removal of organic dyes from waste water using hierarchical NiO spheres with high surface area. J Phys Chem C116:6873–6878